

MRI Reconstruction via Data Driven Markov Chain with Joint Uncertainty Estimation

Guanxiong Luo, ^{*,2}, Martin Heide², and Martin Uecker^{1,2,3,4}

¹Institute of Medical Imaging, Graz University of Technology, Graz, Austria

²Institute for Diagnostic and Interventional Radiology of the University Medical Center Göttingen, Germany

³German Centre for Cardiovascular Research (DZHK), Partner Site Göttingen, Germany

⁴Cluster of Excellence “Multiscale Bioimaging: from Molecular Machines to Networks of Excitable Cells” (MBExC), University of Göttingen, Germany

October 11, 2024

Abstract

We introduce a framework that enables efficient sampling from learned probability distributions for MRI reconstruction. Different from conventional deep learning-based MRI reconstruction techniques, samples are drawn from the posterior distribution given the measured k-space using the Markov chain Monte Carlo (MCMC) method. In addition to the maximum a posteriori (MAP) estimate for the image, which can be obtained with conventional methods, the minimum mean square error (MMSE) estimate and uncertainty maps can also be computed. The data-driven Markov chains are constructed from the generative model learned from a given image database and are independent of the forward operator that is used to model the k-space measurement. This provides flexibility because the method can be applied to k-space acquired with different sampling schemes or receive coils using the same pre-trained models. Furthermore, we use a framework based on a reverse diffusion process to be able to utilize advanced generative models. The performance of the method is evaluated on an open dataset using 10-fold accelerated acquisition.

Keywords – Image reconstruction, Inverse problems, Bayesian inference, Markov chain Monte Carlo, Generative modeling, Posterior sampling

1 Introduction

Modern Magnetic Resonance Imaging (MRI) formulates reconstruction from raw data in Fourier space (k-space) as an inverse problem. Undersampling to reduce acquisition time then leads to an ill-posed reconstruction problem. To solve this problem, parallel imaging can exploit spatial information from multiple receive coils in an extended forward model [1]. Compressed sensing uses the sparsity of images in a transform domain (i.e. wavelet domain, finite differences) as prior knowledge. Combined with incoherent sampling this allows recovery of sparse images from highly undersampled data [2,3]. In recent years, the application of machine learning (ML) pushed these ideas forward by integrating learned prior knowledge.

Most of these methods can be classified into two categories: First, methods that unroll the existing iterative reconstruction algorithms into a neural network and train their parameters by maximizing the similarity to a ground truth. In [4], the authors replaced the handcrafted regularization term with convolution layers, and derived a neural network from the iterative procedure of the Alternating Direction Method of Multipliers (ADMM) algorithm. [5, 6] investigated similar approaches. The downside of this kind of method is the need for supervised training, which requires raw k-space data with fixed known sampling patterns and corresponding ground truth images. The second category consists of methods that learn a prior from high-quality images, then plug it into existing iterative algorithms as a regularization term. In [7–9], the image prior was constructed with a variational auto-encoder [10], a denoising auto-encoder [11] and an autoregressive generative model [12], respectively. These methods then compute a maximum a posterior (MAP) as the estimator of the image. These

^{*}Guanxiong Luo, University Medical Center Göttingen, Institute for Diagnostic and Interventional Radiology, Robert-Koch-Str. 40, 37075 Göttingen, Germany guanxiong.luo@med.uni-goettingen.de

types of methods separate the learned information from the encoding matrix (sampling pattern in k-space and coil sensitivities), which permits more flexibility in practice because they allow the acquisition patterns and receive coils to change without retraining. Generative adversarial networks were also used for image reconstruction in [13]. There, the discriminator is used to confine the space of the output of a generator that is designed to generate images with conformity to k-space data.

Although ML-based approaches provide promising results, worries about the uncertainty caused by undersampling strategies and algorithms have limited their usage in clinical practice until now. Therefore, the uncertainty assessment constitutes an important step for DL-based approaches. The uncertainty is two-fold: 1) the uncertainty of weights inside the neural network [14, 15]; and 2) the uncertainty introduced by the missing k-space data points. The uncertainty from missing k-space data points can be addressed in a Bayesian estimation framework. In [8, 14], the MAP estimator is used, but it provides only the mode of the posterior density $p(\mathbf{x}|\mathbf{y})$ and practical optimization may also even only provide a local maximum. In the setting of Bayesian inference, it is possible to investigate the full shape of posterior distribution $p(\mathbf{x}|\mathbf{y})$. In particular, it is possible to draw sample from the posterior distribution using the Markov chain Monte Carlo (MCMC) method, which was recently exploited for image reconstruction using machine learning in MRI [16].

To be able to utilize more sophisticated generative priors, we developed a generic framework for MRI reconstruction, based on a series of publications related to generative models [17–21], in which the essential idea is to: 1) systematically and slowly destroy the underlying prior knowledge in a data distribution through an iterative forward diffusion process; 2) learn a reverse diffusion process that restores the patterns and 3) incorporate the forward model of the measurement into the learned reverse process. The general picture of the proposed method is illustrated in Figure 1. With efficient MCMC sampling techniques, we explore the posterior distribution $p(\mathbf{x}|\mathbf{y})$ by simulating samples with Algorithm 1. We investigated the proposed method from these perspectives: 1) the interpretation of the uncertainty of the image reconstructed from undersampled k-space; 2) the effect of the number of noise scales used to train the generative models; 3) the effect of using a burn-in phase in MCMC sampling; 4) the distortion due to the weak constraint of k-space data consistency; and 5) the performance on open MRI image dataset.

2 Theory

2.1 Magnetic Resonance Image Reconstruction as Bayesian Inference

We consider image reconstruction as a Bayesian problem where the posterior of image $p(\mathbf{x}|\mathbf{y})$ given with the measured data \mathbf{y} and a prior $p(\mathbf{x})$ learned from a database of images [8]. Here, the image is denoted as $\mathbf{x} \in \mathbb{C}^{n \times n}$, where $n \times n$ is the size of image, and $\mathbf{y} \in \mathbb{C}^{M \times \gamma}$ is the vector of M complex-valued k-space samples from γ receive coils. Assuming the noise η circularly-symmetric normal with zero mean and covariance matrix Γ , the likelihood $p(\mathbf{y}|\mathbf{x})$ for observing the \mathbf{y} determined by $\mathbf{y} = \mathcal{A}\mathbf{x} + \eta$ and given the image \mathbf{x} is given by a complex normal distribution

$$\begin{aligned} p(\mathbf{y}|\mathbf{x}) &= \mathcal{CN}(\mathbf{y}; \mathcal{A}\mathbf{x}, \Gamma) \\ &= \det(\pi\Gamma)^{-\frac{1}{2}} e^{-\|\Gamma^{-\frac{1}{2}}(\mathbf{y} - \mathcal{A}\mathbf{x})\|_2^2} \end{aligned} \quad (1)$$

Here, $\mathcal{CN}(\mathbf{y}; \mathbf{x}, \Gamma)$ denotes a normal distribution with mean \mathbf{x} and covariance matrix Γ (and zero relation matrix). In the following, we assume $\Gamma = \sigma_\eta^2 \mathbf{I}$, where \mathbf{I} is the identity matrix and σ_η the standard deviation of the noise. \mathcal{A} is the forward operator and given by $\mathcal{A} = \mathcal{P}\mathcal{F}\mathcal{S}$, where $\mathcal{S} : \mathbb{C}^{n \times n} \rightarrow \mathbb{C}^{n \times n \times \gamma}$ are the coil sensitivity maps, $\mathcal{F} : \mathbb{C}^{n \times n \times \gamma} \rightarrow \mathbb{C}^{n \times n \times \gamma}$ the two-dimensional Fourier transform, and $\mathcal{P} : \mathbb{C}^{n \times n \times \gamma} \rightarrow \mathbb{C}^{M \times \gamma}$ the k-space sampling operator. According to Bayes' theorem the posterior density function $p(\mathbf{x}|\mathbf{y})$ is then

$$p(\mathbf{x}|\mathbf{y}) = \frac{p(\mathbf{y}|\mathbf{x}) \cdot p(\mathbf{x})}{p(\mathbf{y})}. \quad (2)$$

In this work, the reconstruction is based on the sampling of this posterior distribution. We utilize an efficient technique based on the Markov Chain Monte Carlo method with the application of a diffusion probabilistic generative model. This consists of two processes: 1) a forward diffusion process which converts a complicated distribution used as prior for the image into a simple Gaussian distribution; and 2) a learned finite-time reversal of this diffusion process with which a Gaussian distribution is gradually transformed back to the posterior (cf. Figure 1).

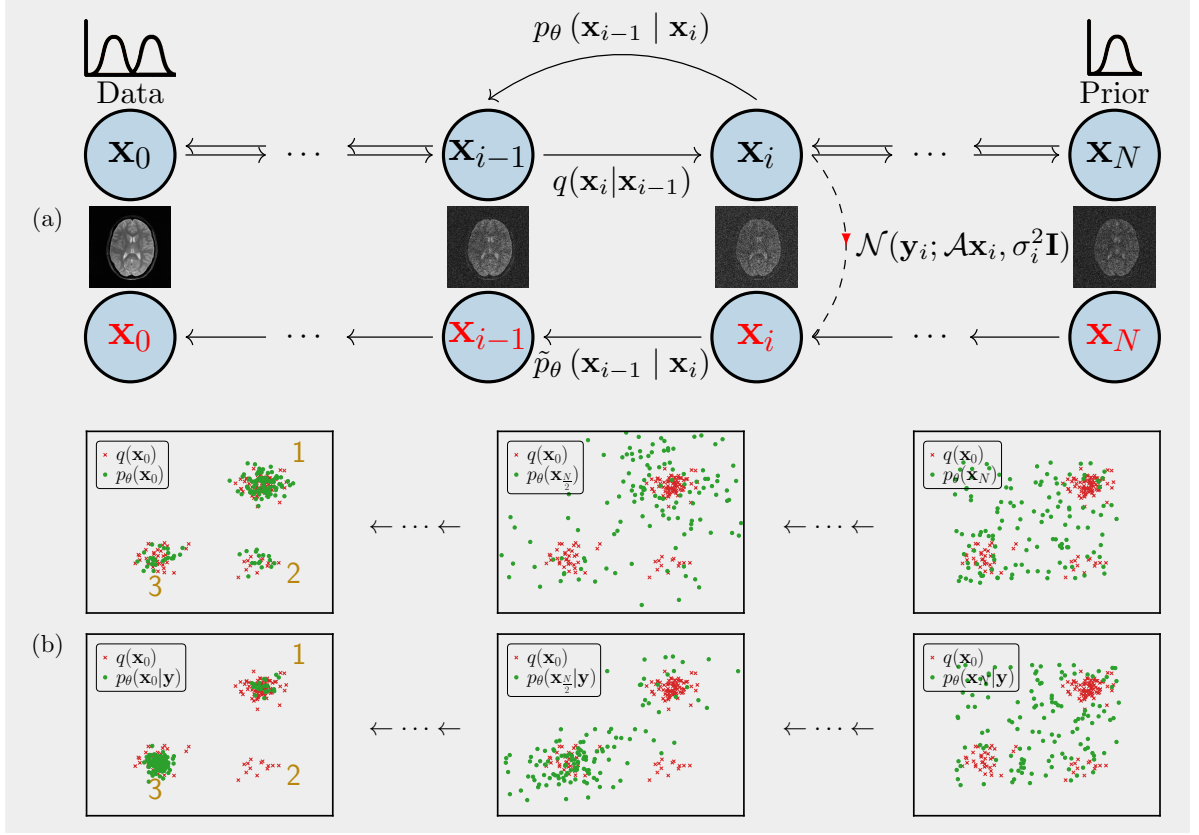


Figure 1. Overview of the proposed method. (a) The data distribution goes through Gaussian diffusion from the left $q(\mathbf{x}_0)$ to the right $q(\mathbf{x}_N)$, and this process is reversed by learned transition kernels $p_\theta(\mathbf{x}_{i-1} | \mathbf{x}_i)$. To compute the posterior of the image $p(\mathbf{x}|\mathbf{y})$, a new Markov chain $\tilde{p}_\theta(\mathbf{x}_{i-1} | \mathbf{x}_i)$ is constructed with the measurement model and the learned reverse. (b) The simulation with the mixture of bivariate Gaussian distribution. The higher and lower reverse processes illustrate how simulating samples (green dots) gradually gather around true samples (red dots) without and with observation \mathbf{y} , respectively. The observation indicates that dots are not from the 2nd cluster and more likely from the 3rd cluster.

2.2 The Forward Diffusion Process

In probabilistic diffusion models, the data distribution characterized by density $q(\mathbf{x}_0)$ is gradually converted into an analytically tractable distribution (Gaussian noise). The image \mathbf{x}_0 is perturbed with a sequence of noise scales $0 = \sigma_0 < \sigma_1 < \dots < \sigma_N$. When the number of steps used for discretization $N \rightarrow \infty$, the diffusion process becomes a continuous process. Here, we consider the discrete Markov chain

$$\mathbf{x}_i = \mathbf{x}_{i-1} + \mathbf{z}_{i-1}, \quad i = 1, \dots, N. \quad (3)$$

where $\mathbf{z}_{i-1} \sim \mathcal{CN}(\mathbf{0}, (\sigma_i^2 - \sigma_{i-1}^2)\mathbf{I})$, i.e. the i -th transition kernel is then given by

$$q(\mathbf{x}_i | \mathbf{x}_{i-1}) = \mathcal{CN}(\mathbf{x}_i; \mathbf{x}_{i-1}, (\sigma_i^2 - \sigma_{i-1}^2)\mathbf{I}). \quad (4)$$

Instead of doing transitions step by step [21, 22] during the training stage, the perturbation kernel derived from Equation (4) is

$$q(\mathbf{x}_i | \mathbf{x}_0) = \mathcal{CN}(\mathbf{x}_i; \mathbf{x}_0, \sigma_i^2 \mathbf{I}) \quad (5)$$

as a convolution of Gaussians. With Bayes' theorem we can write:

$$q(\mathbf{x}_{i-1} | \mathbf{x}_i, \mathbf{x}_0) = q(\mathbf{x}_i | \mathbf{x}_{i-1}) \frac{q(\mathbf{x}_{i-1} | \mathbf{x}_0)}{q(\mathbf{x}_i | \mathbf{x}_0)}. \quad (6)$$

Given the initial image \mathbf{x}_0 , the posterior of a single step of the forward process is then given by (see Appendix A)

$$q(\mathbf{x}_{i-1} | \mathbf{x}_i, \mathbf{x}_0) = \mathcal{CN}(\mathbf{x}_{i-1}; \frac{\sigma_{i-1}^2}{\sigma_i^2} \mathbf{x}_i + (1 - \frac{\sigma_{i-1}^2}{\sigma_i^2}) \mathbf{x}_0, \tau_i^2 \mathbf{I}) \quad (7)$$

with variance $\tau_i^2 := (\sigma_i^2 - \sigma_{i-1}^2) (\sigma_{i-1}^2 / \sigma_i^2)$.

2.3 Learning the Reverse Process

The joint distribution of the reversal diffusion process is characterized by the probability density

$$p(\mathbf{x}_N, \mathbf{x}_{N-1}, \dots, \mathbf{x}_0) = p(\mathbf{x}_N) \prod_{i=1}^N p(\mathbf{x}_{i-1} | \mathbf{x}_i), \quad (8)$$

where $p(\mathbf{x}_N)$ is the initial Gaussian distribution. The reverse is given by Kolmogorov's backward equation which has the same form as the forward process [19, 22]. Thus, the transitions $p(\mathbf{x}_{i-1} | \mathbf{x}_i)$ of the reverse process can be parameterized with the Gaussian transition kernel

$$p_{\theta}(\mathbf{x}_{i-1} | \mathbf{x}_i) = \mathcal{CN}(\mathbf{x}_{i-1}; \boldsymbol{\mu}_{\theta}(\mathbf{x}_i, i), \tau_i^2 \mathbf{I}), \quad (9)$$

where $\boldsymbol{\mu}_{\theta}(\mathbf{x}_i, i)$ and $\tau_i^2 \mathbf{I}$ are the mean and variance of the reverse transitions, respectively. Since the reverse transitions $p_{\theta}(\mathbf{x}_{i-1} | \mathbf{x}_i)$ lead to a new density $p(\mathbf{x}_0)$, which should match $q(\mathbf{x}_0)$, they can be learned by minimizing the cross entropy

$$H(p, q) = -\mathbb{E}_{q(\mathbf{x}_0)} [\log p(\mathbf{x}_0)]. \quad (10)$$

Following [19] a lower bound ℓ can be written in terms of KL divergence between the transition kernel Equation (9) and the posterior of forward process Equation (7)

$$\begin{aligned} \ell &= \sum_{i=2}^N \mathbb{E}_{q(\mathbf{x}_0)} \mathbb{E}_{q(\mathbf{x}_i | \mathbf{x}_0)} [D_{\text{KL}}(q(\mathbf{x}_{i-1} | \mathbf{x}_i, \mathbf{x}_0) \| p_{\theta}(\mathbf{x}_{i-1} | \mathbf{x}_i))] \\ &= \sum_{i=2}^N \mathbb{E}_{q(\mathbf{x}_0)} \mathbb{E}_{q(\mathbf{x}_i | \mathbf{x}_0)} \left[\frac{1}{\tau_i^2} \left\| \frac{\sigma_{i-1}^2}{\sigma_i^2} \mathbf{x}_i + \left(1 - \frac{\sigma_{i-1}^2}{\sigma_i^2}\right) \mathbf{x}_0 - \boldsymbol{\mu}_{\theta}(\mathbf{x}_i, i) \right\|_2^2 \right] + C, \end{aligned} \quad (11)$$

where C is a constant. The derivation of KL divergence between two Gaussians is detailed in Appendix B. Using Equation (5) we can express $\mathbf{x}_i = \mathbf{x}_0 + \mathbf{z}$ with $\mathbf{z} \sim \mathcal{CN}(\mathbf{0}, \sigma_i^2 \mathbf{I})$, and obtain

$$\ell = \sum_{i=2}^N \mathbb{E}_{\mathbf{x}_0, \mathbf{z}} \left[\frac{1}{\tau_i^2} \left\| \frac{\sigma_{i-1}^2}{\sigma_i^2} \mathbf{z} + \mathbf{x}_0 - \boldsymbol{\mu}_{\theta}(\mathbf{x}_i, i) \right\|_2^2 \right] + C. \quad (12)$$

Thus, we can learn the mean of the reverse transitions by learning to denoise the training data disturbed by noise. In [17, 18], the generative model is estimated by minimizing the expected squared distance between the gradient of the log-probability given by the score network and the gradient of the log-probability of the observed data. This technique was extended and generalized in [20, 21]. In the following, we quickly point out the connection to score denoising networks. Let:

$$\boldsymbol{\mu}_{\theta}(\mathbf{x}_i, i) - \mathbf{x}_0 = \sigma_{i-1}^2 \mathbf{s}_{\theta}(\mathbf{x}_i, i), \quad (13)$$

where $\mathbf{s}_{\theta}(\mathbf{x}_i, i)$ denotes the score network that is conditional on the index of noise scales i . Then, we have

$$\ell = \sum_{i=2}^N \mathbb{E}_{\mathbf{x}_0, \mathbf{z}} \left[\frac{\sigma_{i-1}^2}{\tau_i^2} \left\| \frac{\mathbf{z}}{\sigma_i^2} - \mathbf{s}_{\theta}(\mathbf{x}_i, i) \right\|_2^2 \right] + C. \quad (14)$$

Expressing the noise again as $\mathbf{z} = \mathbf{x}_i - \mathbf{x}_0$, we can rewrite

$$\mathbb{E}_{\mathbf{x}_0, \mathbf{z}} \left[\left\| \frac{\mathbf{x}_0 - \mathbf{x}_i}{\sigma_i^2} - \mathbf{s}_{\theta}(\mathbf{x}_i, i) \right\|_2^2 \right] = \mathbb{E}_{q(\mathbf{x}_0)} \mathbb{E}_{q(\mathbf{x}_i | \mathbf{x}_0)} \left[\left\| \nabla_{\mathbf{x}_i} \log q(\mathbf{x}_i | \mathbf{x}_0) - \mathbf{s}_{\theta}(\mathbf{x}_i, i) \right\|_2^2 \right] \quad (15)$$

which shows that Equation (14) is equivalent to score matching. For the later use of the transition kernel, Equation (13) is equivalent to

$$\boldsymbol{\mu}_{\theta}(\mathbf{x}_i, i) - \mathbf{x}_i = (\sigma_i^2 - \sigma_{i-1}^2) \mathbf{s}_{\theta}(\mathbf{x}_i, i). \quad (16)$$

2.4 Computing the Posterior for MRI Reconstruction

In order to compute the posterior probability $p(\mathbf{x}|\mathbf{y})$ for the image \mathbf{x} given the data \mathbf{y} , we need to modify the learned reverse process. We can achieve this by multiplying each of the intermediate distributions $p(\mathbf{x}_i)$ with the likelihood term $p(\mathbf{y}|\mathbf{x}_i)$. We use $\tilde{p}(\mathbf{x}_i)$ to denote the resulting sequence of intermediate distributions

$$\tilde{p}(\mathbf{x}_i) \propto p(\mathbf{x}_i) p(\mathbf{y}|\mathbf{x}_i) \quad (17)$$

up to the unknown normalization constant. Following [19], the transition from \mathbf{x}_{i+1} to \mathbf{x}_i of the modified reverse process is

$$\tilde{p}(\mathbf{x}_i | \mathbf{x}_{i+1}) \propto p(\mathbf{x}_i | \mathbf{x}_{i+1}) p(\mathbf{y}|\mathbf{x}_i). \quad (18)$$

According to Equation (1), we have

$$p(\mathbf{y}|\mathbf{x}_i) = \mathcal{CN}(\mathbf{y}; \mathcal{A}\mathbf{x}_i, \sigma_\eta^2 \mathbf{I}). \quad (19)$$

The sampling at each intermediate distribution of Markov transitions Equation (18) is performed with the unadjusted Langevin Monte Carlo [23]

$$\mathbf{x}_i^{k+1} \leftarrow \mathbf{x}_i^k + \frac{\gamma}{2} \nabla_{\mathbf{x}_i} \log \tilde{p}(\mathbf{x}_i^k | \mathbf{x}_{i+1}) + \sqrt{\gamma} \mathbf{z}, \quad (20)$$

where \mathbf{z} is standard complex Gaussian noise $\mathcal{CN}(0, \mathbf{I})$. With the learned reverse process $p_{\theta}(\mathbf{x}_i | \mathbf{x}_{i+1})$, the log-derivative of $\tilde{p}_{\theta}(\mathbf{x}_i | \mathbf{x}_{i+1})$ with respect to \mathbf{x}_i is

$$\nabla_{\mathbf{x}_i} \log \tilde{p}_{\theta}(\mathbf{x}_i | \mathbf{x}_{i+1}) = \nabla_{\mathbf{x}_i} \log p_{\theta}(\mathbf{x}_i | \mathbf{x}_{i+1}) + \nabla_{\mathbf{x}_i} \log p(\mathbf{y}|\mathbf{x}_i), \quad (21)$$

where

$$\nabla_{\mathbf{x}_i} \log p_{\theta}(\mathbf{x}_i | \mathbf{x}_{i+1}) = \frac{1}{\tau_{i+1}^2} (\sigma_{i+1}^2 - \sigma_i^2) \mathbf{s}_{\theta}(\mathbf{x}_{i+1}, i) \quad (22)$$

and

$$\nabla_{\mathbf{x}_i} \log p(\mathbf{y}|\mathbf{x}_i) = -\frac{1}{\sigma_\eta^2} (\mathcal{A}^H \mathcal{A} \mathbf{x}_i - \mathcal{A}^H \mathbf{y}_0). \quad (23)$$

According to Equation (20), each iteration is

$$\mathbf{x}_i^{k+1} \leftarrow \mathbf{x}_i^k + \left[\frac{\gamma}{2\tau_{i+1}^2} (\sigma_{i+1}^2 - \sigma_i^2) \mathbf{s}_{\theta}(\mathbf{x}_i^k, i) - \frac{\gamma}{2\sigma_\eta^2} (\mathcal{A}^H \mathcal{A} \mathbf{x}_i^k - \mathcal{A}^H \mathbf{y}_0) \right] \Big|_{\mathbf{x}_i^0 = \mathbf{x}_{i+1}^K} + \sqrt{\gamma} \mathbf{z}. \quad (24)$$

\mathbf{x}_{i+1}^K is from the previous distribution $\tilde{p}(\mathbf{x}_{i+1} | \mathbf{x}_{i+2})$ after K Langevin steps and is used as the initial point for $\tilde{p}(\mathbf{x}_i | \mathbf{x}_{i+1})$ and so on. We found it advantageous to modify the likelihood term in each step according $\sigma_\eta^2 = \tau_{i+1}/\lambda$, which should approach the variance of the data noise in the last step. Since the noise variance was unknown for the data set we used, we empirically selected a λ . We set γ to $2\tau_{i+1}^2$. At last, the algorithm used to sample the posterior is in Algorithm 1.

Algorithm 1 Sampling the posterior via Markov chain Monte Carlo

- 1: Give the acquired k-space \mathbf{y} .
- 2: Construct the forward operator \mathcal{A} with sampling pattern \mathcal{P} and coil sensitivities \mathcal{S} .
- 3: Set the Langevin steps K , the factor λ , the start noise level index N , and γ .
- 4: Generate \mathbf{x}_N^0 from a Gaussian distribution with the zero mean and σ_N^2 variance.
- 5: **for** i in $\{N-1, \dots, 0\}$ **do**
- 6: Draw samples from $\tilde{p}(\mathbf{x}_i | \mathbf{x}_{i+1})$ by running K Langevin steps with Equation (24).
- 7: **end for**

To characterize shape of posterior, we run multiple chains to draw samples in parallel. To reduce the amount of computation, the burn-in phase is introduced as shown in Figure 2. That means only one chain proceeds through the several beginning noise levels, and after that we spawn multiple Markov chains using the burned sample as initial point indicated by the green dot. To further reduce computation, we introduce the continuously decreasing noise scales, which reduces the number of iterations when performing Langevin dynamics at each intermediate distribution.

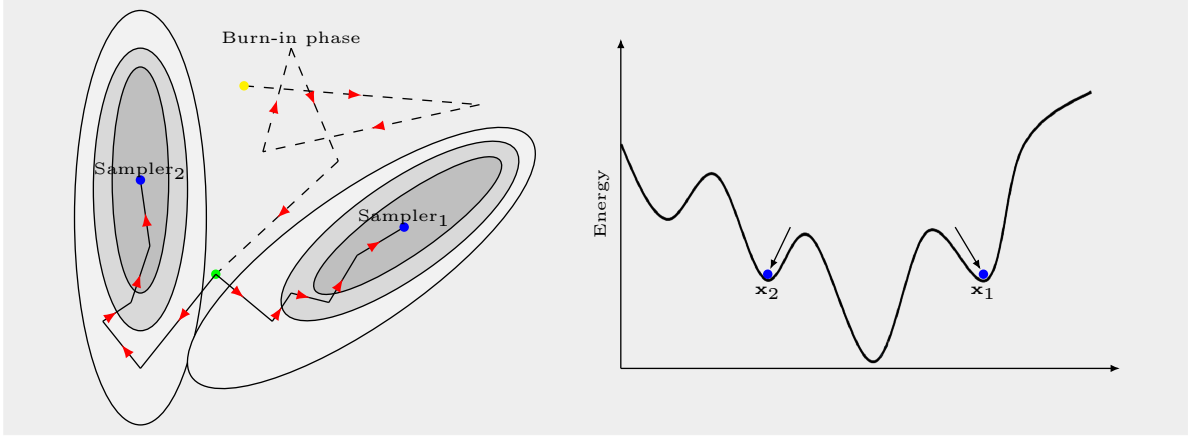


Figure 2. Illustration for the sampling process of MCMC. (a) The burn-in phase is indicated by dashed lines and two possible sampling trajectories reach to two local optimal solutions. (b) Two possible optimal solutions have the comparable amount of energy.

2.5 The Analysis of Samples

Given a posterior probability distribution $p(\mathbf{x}|\mathbf{y})$ the minimum mean square error (MMSE) estimator minimizes the mean square:

$$\mathbf{x}_{\text{MMSE}} = \arg \min_{\tilde{\mathbf{x}}} \int \|\tilde{\mathbf{x}} - \mathbf{x}\|^2 p(\mathbf{x}|\mathbf{y}) d\mathbf{x} = \mathbb{E}[\mathbf{x}|\mathbf{y}]. \quad (25)$$

The above expectation can be used as an estimate for the image. We can approximate it by averaging the samples computed using MCMC procedure. The variance of the samples is a solution to the error assessment for the reconstruction if we trust the model parameterized by Equation (9) that is learned from image database.

3 Methods

3.1 Score Networks' Architecture

For a discrete model, we added the modified instance normalization layers that are conditional on the index of noise scales following convolution layers. The conditional instance normalization [24] is

$$\mathbf{z}_k = \Phi[i, k] \frac{\mathbf{x}_k - \mu_k}{s_k} + \Omega[i, k], \quad (26)$$

where $\Phi \in \mathbb{R}^{N \times C}$ and $\Omega \in \mathbb{R}^{N \times C}$ are learnable parameters, k denotes the index of feature maps, μ_k and s_k are the means and standard deviation of feature maps, and i denotes the index of σ in $\{\sigma_i\}_{i=1}^N$.

For a continuous model, we let networks be conditional on the index of noise scales by inserting random fourier features [25]. Three steps used to encode a noise index into random features are as follows:

- Draw a random vector which has i.i.d. Gaussian m entries with the specified standard deviation,
- Scale the random vector with the index i , then multiply it with 2π ,
- Apply sines and cosines to the scaled random vector, then concatenate them into $m \times 2$ matrix,

where m is embedding size. The encoded index is added to all the blocks in a neural network, e.g., a conditional residual block or a conditional refine block.

With the above two modifications, both score networks $\mathbf{s}_\theta(\mathbf{x}, i)$ can take two inputs image \mathbf{x} and noise index i . RefineNet [26] is the backbone of all the score networks used in this work. Three variants from that are trained for different reconstruction experiments. For the ease of reference, we labeled them with NET_1 , NET_2 , NET_3 , respectively. NET_1 is conditional on discrete noise scales, NET_2 and NET_3 are conditional on continuous noise scales. We introduce self-attention modules into NET_3 to capture long-range dependencies [27] so that the network have capability to model the dataset of images of high-resolution. The architectures of three networks are presented in detail in Appendix C. Besides, the sequence of noise scales $\{\sigma_i\}_{i=1}^N$ is geometrically generated following the scheme in [20].

3.2 Dataset, Training and Inference

The dataset used in [8] has 1300 images containing T1-weighted, T2-weighted, T2-weighted fluid-attenuated inversion recovery (FLAIR), and T2*-weighted brain images from 13 healthy volunteers examined with clinical standard-of-care protocols. The brain images from fastMRI [28] dataset were used for benchmark that contains T1-weighted (some have post contrast), T2-weighted and FLAIR images. For the detailed information of both dataset, we refer readers to corresponding publication. Regarding the data partitioning, we first separated all multi-slice volumes into training and testing groups. Then we split the volume into slices (i.e., images). Training images were reconstructed from multi-channel k-space data without undersampling. Then, these complex image datasets after coil combination were scaled to a magnitude range of $[-1, 1]$ without losses of phase information. The coil sensitivity maps were computed with BART toolbox using ESPIRiT [29, 30]. During the training, real and imaginary parts of all images were separated into two real and imaginary channel when input into the neural network. 1300 images of size 256×256 from the dataset used in [8] were used to train NET_1 and NET_2 . 1000 images were used for training, and 300 images were used for testing. For the training of NET_3 , we used the FLAIR contrast images of size 320×320 that are reconstructed from fastMRI raw k-space data. 2937 images are for training, 326 images are for testing. To clarify here, the images are denoted with \mathbf{x}_0 in Theory section.

In the implementation, an image \mathbf{x} is treated as a set of $Np = n \times n \times 2$ real Gaussian random variables with covariance matrix $\sigma^2 \mathbf{I}$, the joint probability density function is $p(\mathbf{x}) = 1/\sqrt{(2\pi\sigma^2)^{Np}} \exp(-\|\mathbf{x} - \boldsymbol{\mu}\|^2/2\sigma^2)$.

Three conditional score networks are implemented with Tensorflow [31]. The hyperparameters used to train the three score networks are listed in Appendix D. With the trained networks, we implemented MCMC sampling Algorithm 1 with Tensorflow and Numpy [32], and then explored the posterior $p(\mathbf{x}|\mathbf{y})$ in different experimental settings. We trained three score networks once separately for all the experiments we did in this work. These three models can support all experiments performed in this study with variable undersampling patterns, coil sensitivity maps, channel numbers. It took around 43 and 67 seconds, respectively, to train NET_1 and NET_2 for one epoch on one Tesla A100. For NET_3 , it took around 500 seconds per epoch on two Tesla A100. In the spirit of reproducible research, codes and data to reproduce all experiments are made available on this webpage¹.

3.3 Experiments

Single Coil Unfolding: To investigate how the Markov chain explores the solution space of the inverse problem $\mathbf{y} = \mathcal{A}\mathbf{x} + \eta$, we designed the single coil unfolding experiment. The single channel k-space is simulated out of multi-channel k-space data. The odd lines in k-space are retained. 10 samples were drawn from the posterior $p(\mathbf{x}|\mathbf{y})$. NET_1 was used to construct transition kernels and the parameters in Algorithm 1 are $K = 50, N = 10, \lambda = 6$. We redo the experiment with the object shifted to bottom.

Multi-Coil Reconstruction: Multi-channel data points from k-space are randomly picked with variable density poisson disc and the central 20×20 region is fully acquired. The acquisition mask covers 11.8% k-space and the corresponding zero-filled reconstruction is shown Figure 4b. We initialized 10 chains and the \mathbf{x}_{MMSE} was computed using different number of samples. NET_1 was used to construct transition kernels and the parameters in Algorithm 1 are $K = 50, N = 10, \lambda = 13$. To visualize the process of sampling, we use peak-signal-noise-ratio (PSNR in dB) and similarity index (SSIM) as metrics to track intermediate samples. The comparisons are made between the magnitude of \mathbf{x}_{MMSE} and the ground truth $\tilde{\mathbf{x}}$ after normalized with ℓ_2 -norm.

More Noise Scales: To investigate how the number of noise scales influences the proposed method, we reconstructed the image from the undersampled k-space that was used in the multi-coil experiment. NET_2 was used to construct transition kernels and the parameters in Algorithm 1 are $K = 5, N = 70, \lambda = 25$.

Investigation into Burn-in Phase: To investigate the burn-in phase illustrated in Figure 2, we spawned multiple chains at a certain noise scale when drawing samples from the posterior $p(\mathbf{x}|\mathbf{y})$. For instance, let $(\mathbf{x}_{\text{MMSE}}, 60)$ denote the \mathbf{x}_{MMSE} that is computed with 10 samples drawn from $p(\mathbf{x}|\mathbf{y})$ by spawning 10 chains at the 60th noise scale. By changing the spawning point, we got different sets of samples that are from chains of different length and computed the final \mathbf{x}_{MMSE} respectively. We have two sets of \mathbf{x}_{MMSE} that are reconstructed from the undersampled k-space using two sampling patterns separately. The central 20×20 region is obtained and the k-space, outside of the center, is randomly picked up retrospectively (10%, 20%). NET_2 was used to construct Markov transition kernels and the parameters in Algorithm 1 are $K = 5, N = 70, \lambda = 25$.

Investigation into MAP: To investigate the samples around the local minimum, we disabled the disturbance of noises after random inference in last distribution $\tilde{p}(\mathbf{x}_0 | \mathbf{x}_1)$ and ran 100 iterations more to get extended samples. The undersampled k-space in this experiment is the same as the one in the multi-coil experiment. NET_2 was used

¹<https://github.com/mrirecon/spreco>

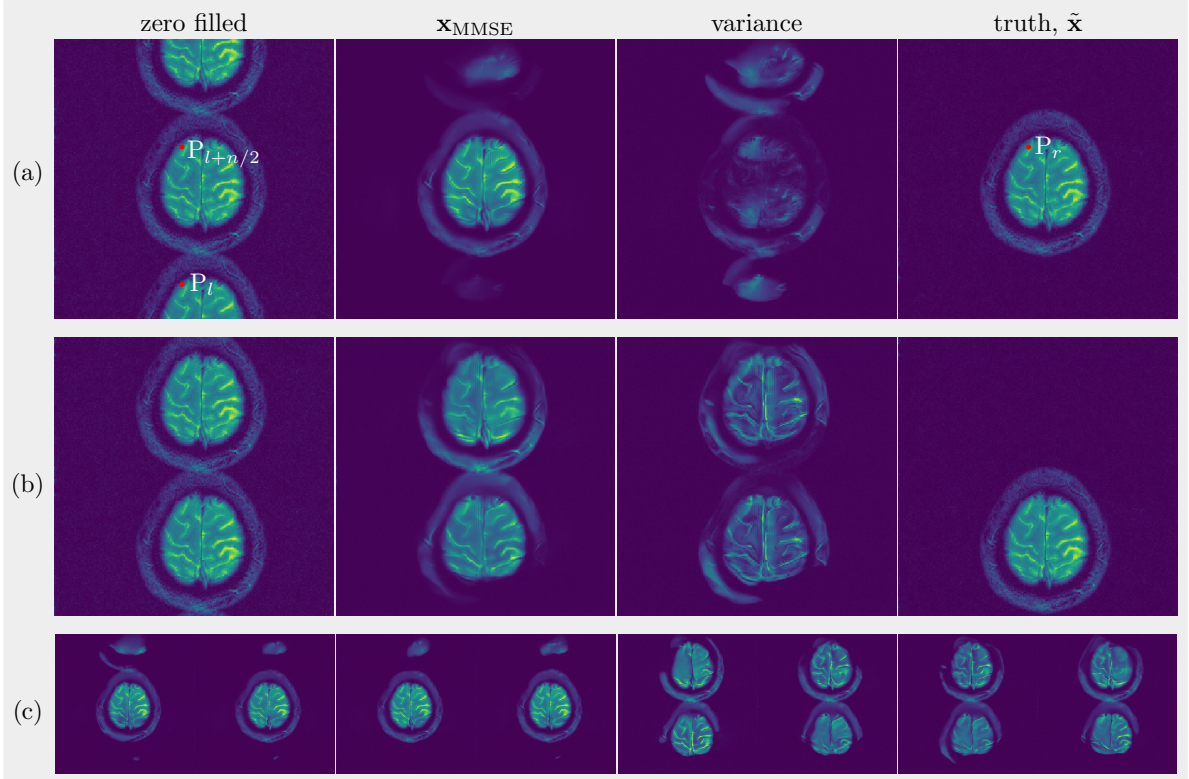


Figure 3. The single coil unfolding ($2 \times$). Aliased images, \mathbf{x}_{MMSE} , variance maps and ground truth are presented. (a) The object is centered. (b) The object is shifted. (c) Selected samples are presented. The left four are centered and the right four are shifted.

to construct transition kernels and the parameters in Algorithm 1 are $K = 5, N = 70, \lambda = 25$. In the extra 100 iterations, we increased λ by 10 times.

Benchmark on Open Dataset: A benchmark using the fastMRI dataset was used to evaluate the performance of the proposed method. We noticed that the raw k-space data is padded with zeros to make them have the same dimension. The effect caused by zero paddings is investigated in [33]. Since we only used the images that were reconstructed from the zero padded k-space for training, the issue caused by the synthesized k-space does not exist in our work. The undersampling pattern for each slice is randomly generated in all retrospective experiments. NET_3 was used to construct transition kernels. The parameters in Algorithm 1 are $K = 3, N = 80, \lambda = 20$ and 10 samples were drawn to compute \mathbf{x}_{MMSE} .

Distortion: To investigate how the tuning factor λ affect the sampling process, we repeated the more noise scales reconstruction experiment with different settings. NET_2 was used to construct transition kernels and the parameters in Algorithm 1 are $K = 2, N = 90, \lambda = \{1, 2, 3, 5, 25\}$.

4 Results

4.1 Single Coil Unfolding

Since there is a lack of spatial information from coil sensitivities, folding artifacts still exist in \mathbf{x}_{MMSE} as shown in Figure 3, even when reconstructed with the learned Markov chains. As only odd lines are acquired, all images in which the superposition of points P_l and $P_{l+n/2}$ equals to the points P_r in ground truth are solutions to $\mathbf{y} = \mathcal{A}\mathbf{x} + \epsilon$ with the same error (the residual norm $\|\mathbf{y} - \mathcal{A}\mathbf{x}\|^2$). The variance map indicates the uncertainty of the estimated reconstruction \mathbf{x}_{MMSE} . As expected, without parallel imaging, uncertainties caused by the undersampling lead to huge errors. The errors of the estimation \mathbf{x}_{MMSE} are largely reduced compared with zero-filled reconstruction, as shown in Figure 3a. The shift of the object increases the symmetry and then leads to even bigger errors as learned Markov chains know less about images that were not shifted (cf. Figure 3b).

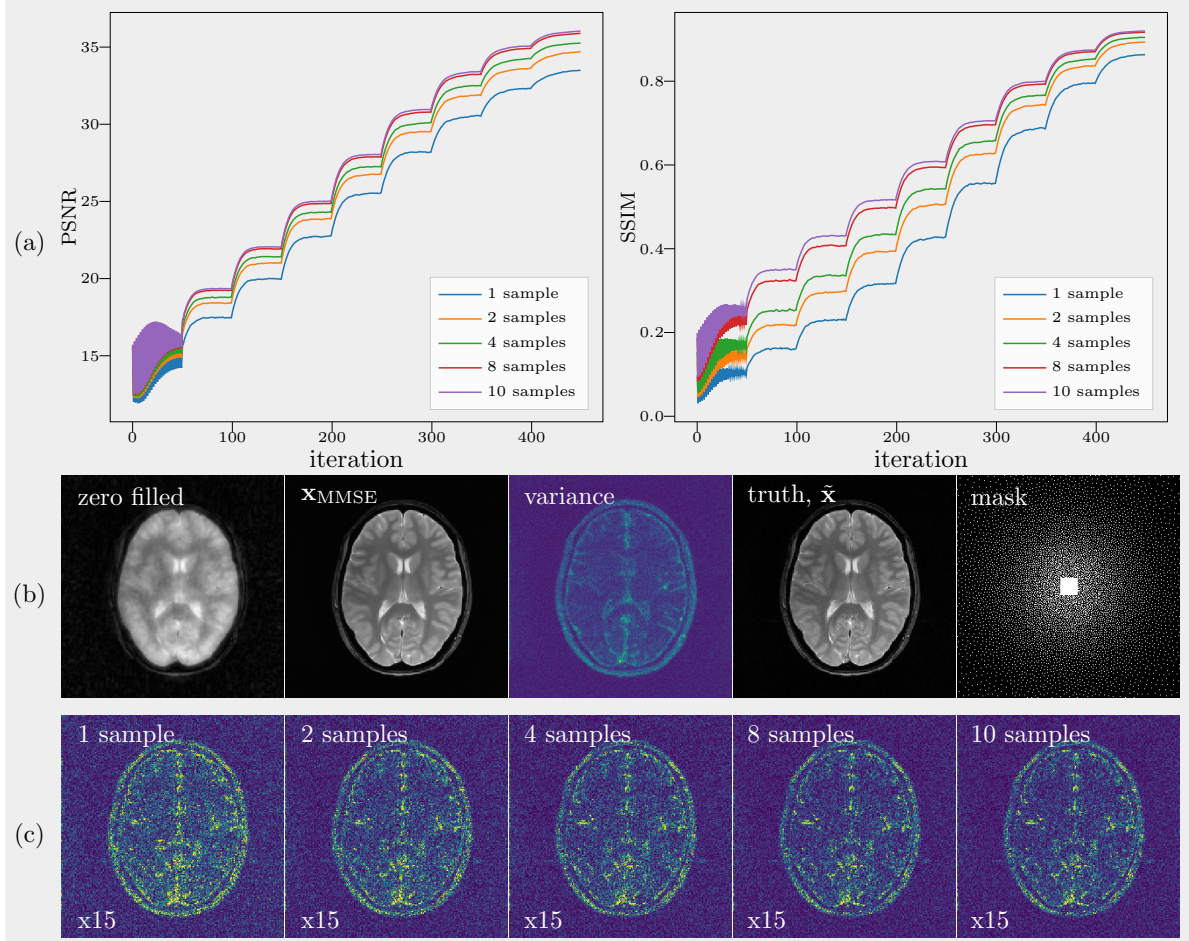


Figure 4. (a) The curves of PSNR and SSIM over iterations. (b) Zero-filled, \mathbf{x}_{MMSE} , variance maps, truth and mask are presented. The PSNR and the SSIM of \mathbf{x}_{MMSE} are 36.03dB and 0.9196, (c) The error maps between different \mathbf{x}_{MMSE} s and the ground truth are presented.

4.2 Multi-Coils Reconstruction

Figure 4 shows the evolution of samples' PSNR and SSIM over the transitions of the data driven Markov chain and intermediate samples are presented in Appendix E. As shown in Figure 4a, the convergence of samples at each noise level was reached indicated by the PSNR and SSIM curves. When the samples are more, the \mathbf{x}_{MMSE} converges to higher PSNR and SSIM. We noticed that the gain gets less and less as the number of chains increases. In Figure 4b, 10 converged samples were used to compute \mathbf{x}_{MMSE} and the variance map. The variance map is calculated over 10 converged samples for each pixel. Comparing with the ground truth, the variance map mainly reflects the edge information, which can be interpreted by the uncertainty that is introduced by the undersampling pattern used in k-space where many high frequency data points are missing but the low frequency data points are fully acquired. In contrast to the single coil unfolding, the local spatial information from coil sensitivities reduce the uncertainties of missing k-space data. Moreover, error maps qualitatively correspond to the variance map, committing larger errors in higher variance regions as shown in Figure 4c, which substantiates that the variance map is an error assessment for the reconstruction. Lastly, the average over more samples commits less errors.

4.3 More Noise Scales

We also plotted the curve of PSNRs and SSIMs over iterations in Figure 5a. The PSNR and SSIM of \mathbf{x}_{MMSE} , which is computed with 10 samples, are 37.21dB and 0.9360. Two \mathbf{x}_{MMSE} reconstructed separately with the application of NET₁ and NET₂ are presented in Figure 5b and variance maps are presented as well. The variance of the samples that are drawn with NET₂ is less than those drawn with NET₁, which means that we are more confident about the reconstruction using NET₂. When we zoom into the region that has more complicated structures, the

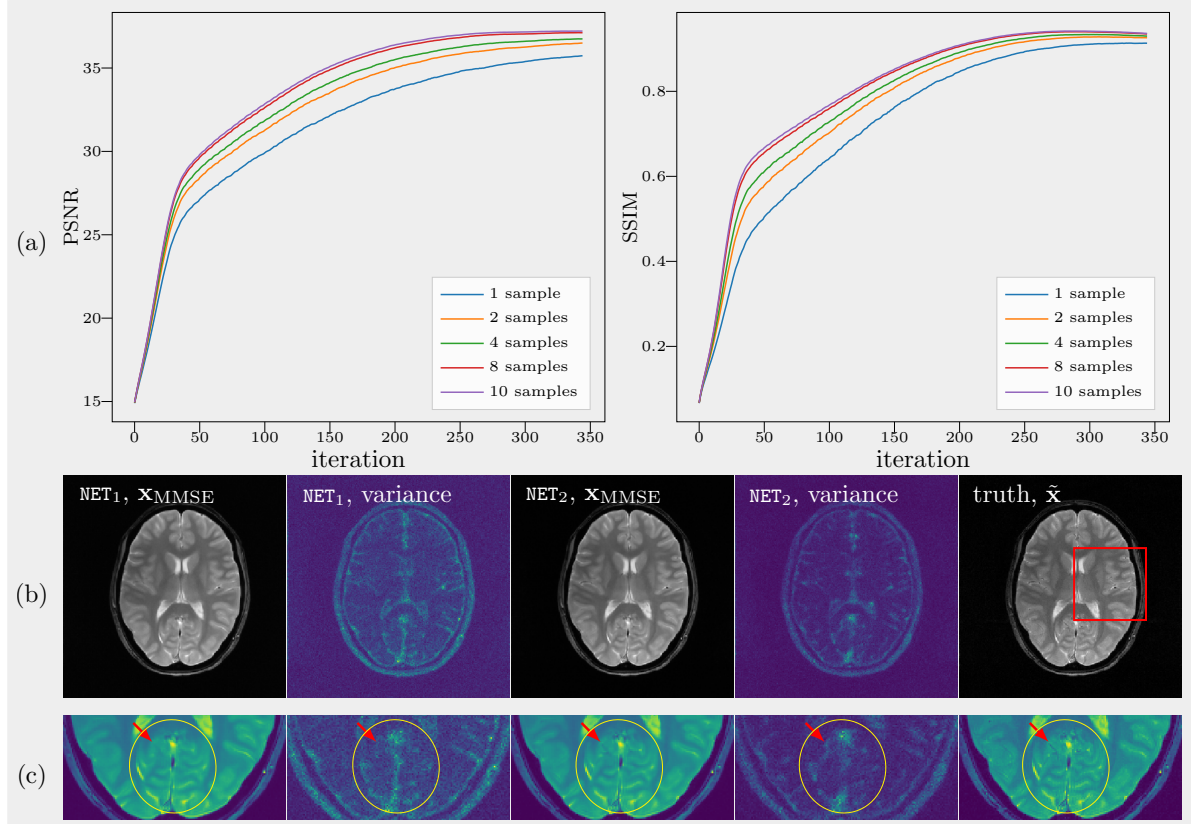


Figure 5. (a) The convergence curves of PSNR and SSIM over iterations. (b) Reconstructions using chains which are constructed with different score networks. (c) Comparisons of complicated structures, highlighted with the yellow circle.

boundaries between white matter and gray matter are more distinct in the image recovered with NET₂ and the details are more obvious, as shown in Figure 5c. Hence, increasing the number of noise scales reduces the number of iterations and improves the quality of reconstruction, using the score networks of comparable size. Hence, we can say that more noise scales make chains constructed with NET₂ exploit the prior knowledge from training image dataset more effectively than chains constructed with NET₁ which has fewer noise scales.

4.4 Investigation into Burn-in Phase

The two sets of \mathbf{x}_{MMSE} are presented in Figure 6. In Figure 6a, the earlier we spawn chains, the closer the \mathbf{x}_{MMSE} gets to the truth. Especially, when we zoom into the region that has complicated structures (indicated by the red rectangle), the longer chains make fewer mistakes. The slightly distorted structure is seen in $(\mathbf{x}_{\text{MMSE}}, 60)$ highlighted with blue circles. The distortion has disappeared in $(\mathbf{x}_{\text{MMSE}}, 0)$ but some details are still missing. However, give more k-space data points, the longer chains do not cause a huge visual difference in the \mathbf{x}_{MMSE} as shown in Figure 6b, even there is a slight increase in PSNR and SSIM. Although fewer data points means more uncertainties, long chains permit more sufficient exploration of the solution space, as evidenced by this experiment, but the benefit of long chains is at the price of more computation. Hence, in the circumstance of a moderate undersampling rate, a burn-in phase is recommended for reducing computation.

4.5 Investigation into MAP

In Figure 7, we plotted the curves of PSNR and SSIM over iterations and presented reconstructions that are from MMSE and MAP estimator respectively. We noticed that the quality of each extended sample is improved if we use PSNR as the metric, but the similarity between extended samples and the ground truth decreased by around 8%. As shown in Figure 7c, the high variance region gets intensified accompanied with artifacts after 100 iterations, while the lower variance region gets weakened. What's more, the average over extended samples doesn't lead to the improvement of \mathbf{x}_{MMSE} . Though the single extended sample is better than the unextended

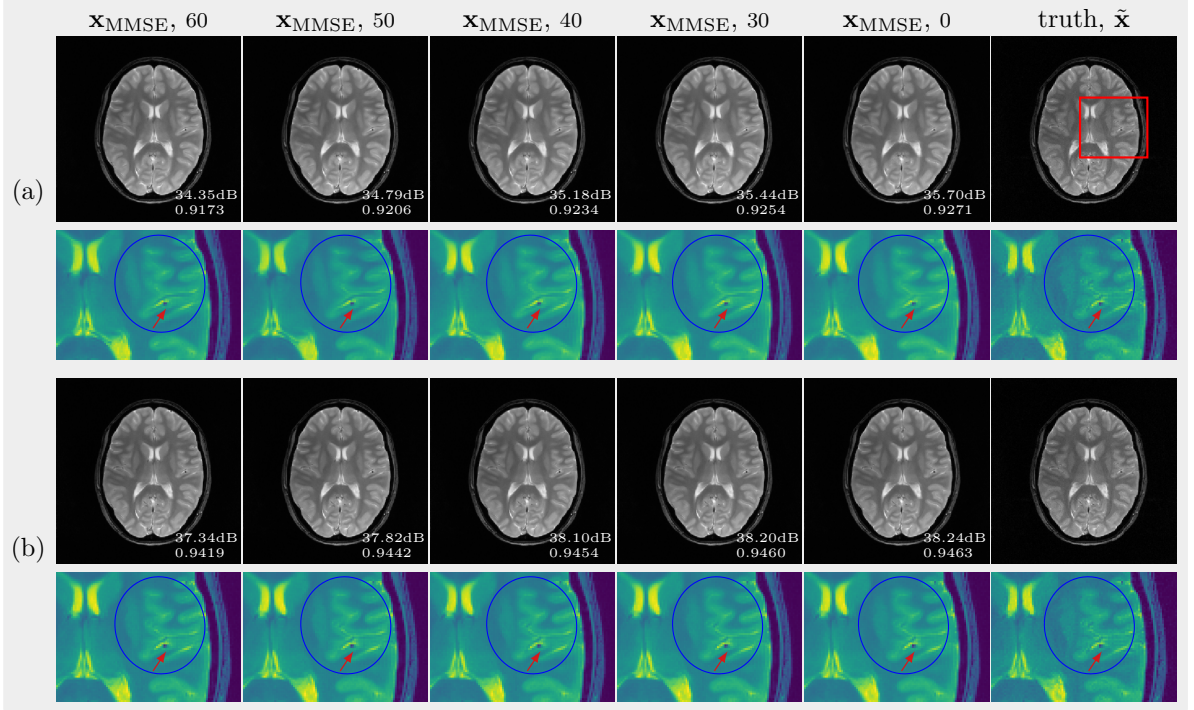


Figure 6. Spawning multiple chains at different time points. (a) 10% k-space data points are obtained. (b) 20% k-space data points are obtained.

Table 1. Average PSNR (dB) and SSIM(%) for test subjects

Sampling rate	ℓ_1 -ESPIRiT			x_MMSE		
	sub ₁	sub ₂	sub ₃	sub ₁	sub ₂	sub ₃
PSNR	32.27	34.67	34.03	34.07	36.12	35.65
10%	33.69	35.60	35.17	35.04	37.15	36.58
SSIM						
10%	79.69	82.74	79.98	84.21	86.06	83.24
20%	83.68	84.60	82.70	86.38	88.26	84.85

sample, they commit visible mistakes in high variance regions and the benefit of averaging over samples get diminished.

4.6 Benchmark on Open Dataset

The selected slice reconstructed with different methods are presented in Figure 8 and other slices is available on this webpage. ℓ_1 -ESPIRiT denotes the reconstruction with the `pics` command of BART toolbox using ℓ_1 -wavelet regularization (0.01), which mostly recovers general structures while smoothing out some details. In x_MMSE, the majority of details are recovered, and the texture is almost identical to the ground truth, although some microscopic structures are still missing. Each subject has 16 slices and the metrics of 3 subjects presented in Table 1 are the average over slices of each subject. It's worth to mention that PSNR and SSIM are more like relative metrics instead of absolute one in the evaluation of MR images.

4.7 Distortion

Figure 9 shows the samples that explore the distribution space with different guidance of data consistency by changing the tuning factor λ . Comparing two samples that are regularized by the small λ , the variation between Figure 9a and Figure 9b is apparent and the distorted samples are far away from the truth. When λ increases, the variation decreases and the distortion disappears, gradually. This is to say, the greater the tuning factor λ , the stronger the constraint applied to the exploration.

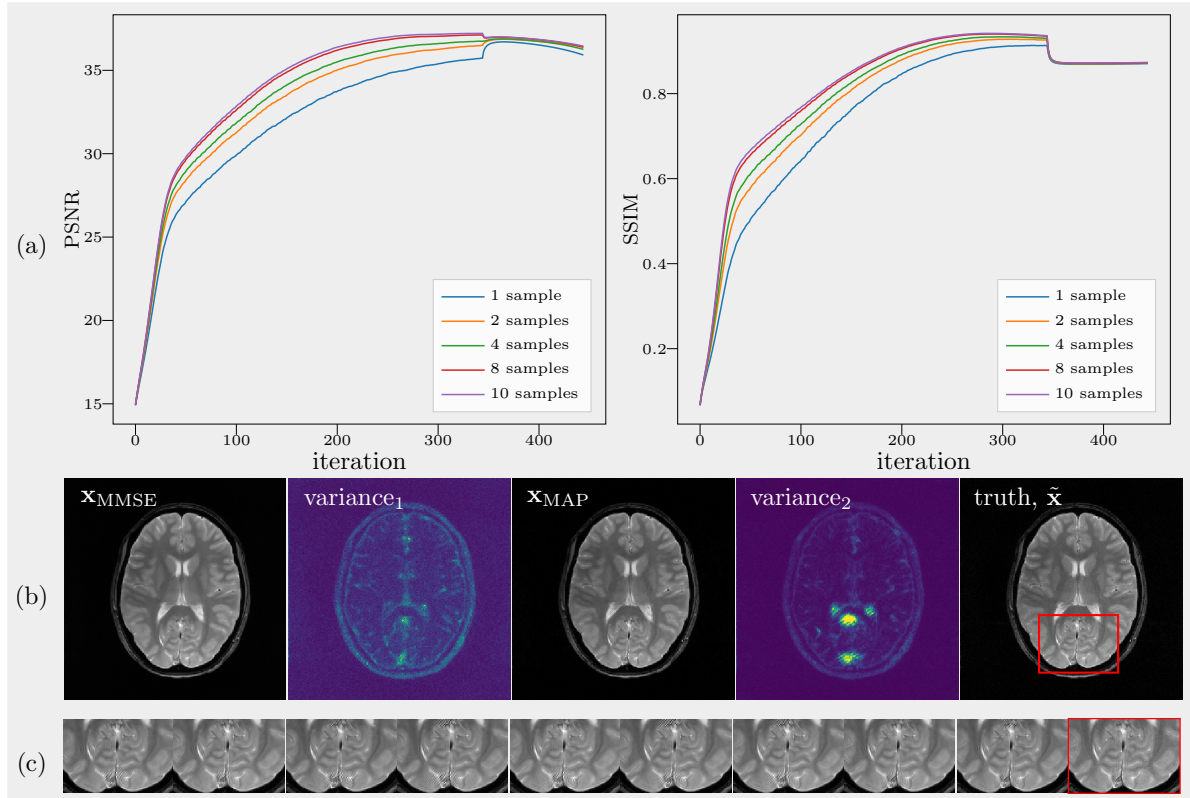


Figure 7. 100 extended MAP iterations after random exploration. (a) The curves of PSNR and SSIM over iterations. (b) The sub-figure variance₁ and variance₂ were computed from unextended samples and extended samples respectively. x_{MAP} is a extended sample. (c) The zoom-in region of 9 extended samples and the ground truth.

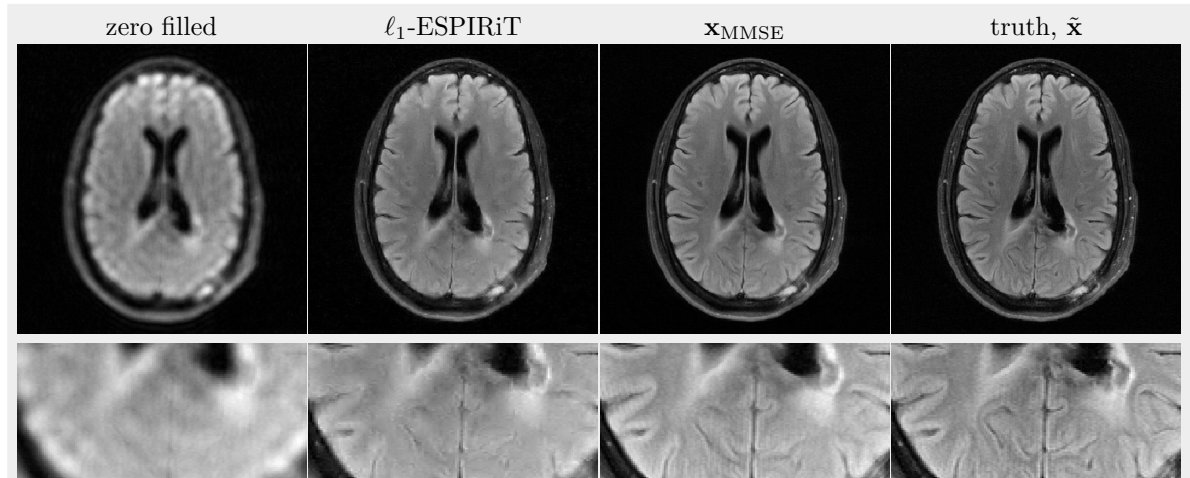


Figure 8. The high resolution image (320×320) reconstructed with the k-space data of 10-fold accelerated acquisition.

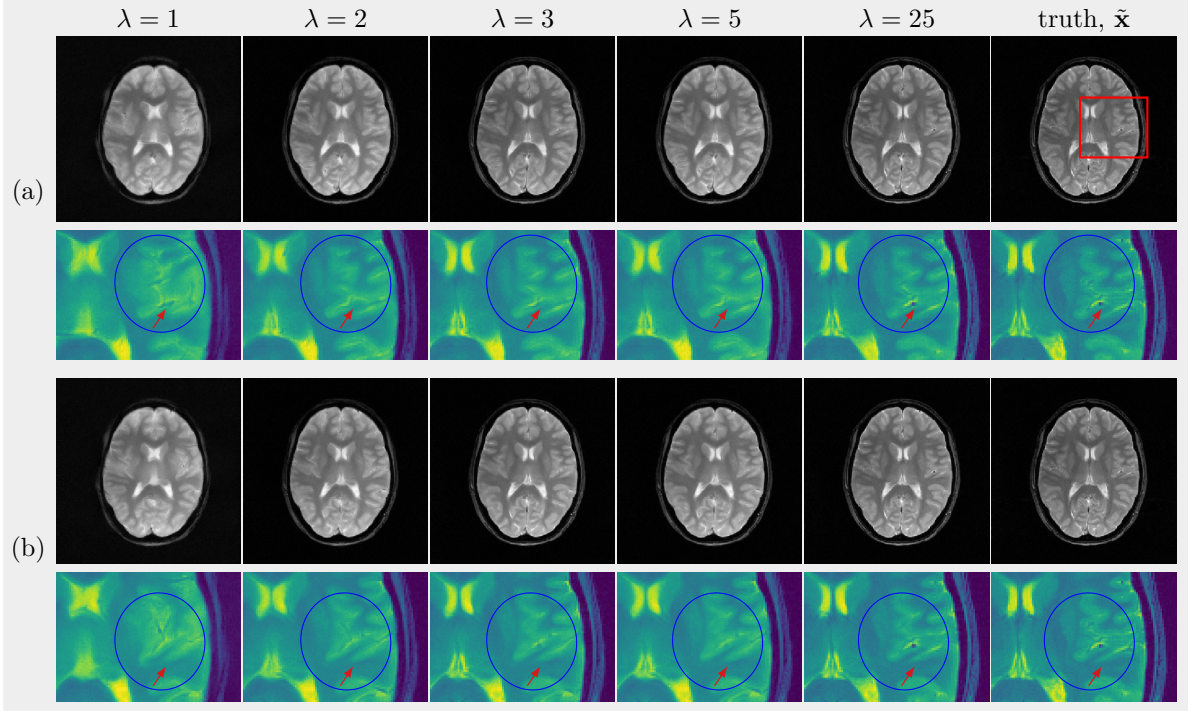


Figure 9. The greater the tuning factor λ , the stricter the constraint applied to the exploration, and vice versa. Two sets of samples are presented in (a) and (b).

5 Discussion

Generally, the Bayesian statistical approach provides a foundation for sampling the posterior $p(\mathbf{x}|\mathbf{y})$ and a natural mechanism for incorporating the prior knowledge that is learned from images. The generative model is used to construct Markov chains to sample the posterior. The utilization of probabilistic generative models allows: 1) flexibility for changing the forward model of measurement; 2) exact sampling from the posterior term $p(\mathbf{x}|\mathbf{y})$; and 3) the estimation of uncertainty due to limited k-space data points.

Uncertainties of Reconstruction: One advantage of the proposed approach over classical deterministic regularization methods is that it allows the quantification of uncertainties of the reconstruction with the variance map. That requires MCMC sampling technique. The loss of spatial information of coils leads to the failure of unfolding, as demonstrated in Section 4.1. The region with aliasing correspond to the high variance areas of the uncertainty map. With multiple coils, the reduction of high frequency data points in k-space leads to the loss of fine details, as demonstrated in Section 4.2. The \mathbf{x}_{MMSE} represents the reconstruction with minimum mean square error and the variance map evaluates the confidence interval of \mathbf{x}_{MMSE} .

Overfitting and Distortion: The proposed algorithm is an iterative refining procedure that starts from generating coarse samples with rich variations under large noise, before converging to fine samples with less variations under small noise. For early iterations of the algorithm, each parameter update mimics stochastic gradient descent; however, as the algorithm approaches a local minimum, the gradient shrinks and the chain produces the samples from the posterior. Lastly, we noticed that the balance between the learned transition and the data consistency plays an important role in the generation of realistic samples, as demonstrated in Figure 9.

Computational Burden: The promising performance of this method comes at the price of demanding computation. It takes around 10 minutes to reproduce the results in Figure 5 while ℓ_1 -ESPIRiT takes about 5 seconds with BART for a single slice. The possible solutions to the computation burden are to: 1) accelerate the inferencing of neural networks; 2) parallelize the sampling process when multiple chains are used; and 3) reduce the number of iterations using more efficient MCMC sampling techniques. Furthermore, reducing the scale of networks is also viable.

Relationship to Generative Models: To our knowledge, the construction of image models to exploit prior knowledge was first introduced in [34] in which the handcrafted model which extracts edge information was used

for image restoration. Following that framework, the learned generic image priors from generative perspective are investigated in [35, 36], which permits more expressive modeling. In the medical imaging field, image priors learned with variational autoencoder [7, 10] and PixelCNN [8, 12] were applied to MRI image reconstruction. Compared with some unrolled network based deep learning image reconstruction methods, the application of image priors is independent of k-space data and coil sensitivities, which permits a more versatile use of the method using different k-space acquisition strategies.

6 Conclusion

The proposed reconstruction method combines concepts from machine learning, Bayesian inference and image reconstruction. In the setting of Bayesian inference, the image reconstruction is realized by drawing samples from the posterior term $p(\mathbf{x}|\mathbf{y})$ using data driven Markov chains, providing a minimum mean square reconstruction and uncertainty estimation. The prior information can be learned from an existing image database, where the generic model based on the diffusion process proposed here allows the use of advanced generative priors.

7 Acknowledgement

We acknowledge funding by the "Niedersächsisches Vorab" funding line of the Volkswagen Foundation. We would like to thank Xiaoqing Wang for his help in preparing this manuscript as well as Christian Holme for help with our computer systems.

References

- [1] K. P. Pruessmann, M. Weiger, P. Boernert, and P. Boesiger. Advances in sensitivity encoding with arbitrary k-space trajectories. *Magn. Reson. Med.*, 46(4):638–651, 2001.
- [2] M. Lustig, D. Donoho, and J. M. Pauly. Sparse MRI: The application of compressed sensing for rapid MR imaging. *Magn. Reson. Med.*, 58(6):1182–1195, 2007.
- [3] K. T. Block, M. Uecker, and J. Frahm. Undersampled radial MRI with multiple coils. Iterative image reconstruction using a total variation constraint. *Magn. Reson. Med.*, 57(6):1086–1098, 2007.
- [4] Yan Yang, Jian Sun, Huibin Li, and Zongben Xu. Deep ADMM-Net for Compressive Sensing MRI. In *Advances in Neural Information Processing Systems*, volume 29. Curran Associates, Inc., 2016.
- [5] H. K. Aggarwal, M. P. Mani, and M. Jacob. MoDL: Model-Based Deep Learning Architecture for Inverse Problems. *IEEE Transactions on Medical Imaging*, 38(2):394–405, 2019.
- [6] Kerstin Hammernik, Teresa Klatzer, Erich Kobler, Michael P. Recht, Daniel K. Sodickson, Thomas Pock, and Florian Knoll. Learning a variational network for reconstruction of accelerated MRI data. *Magn. Reson. Med.*, 79(6):3055–3071, 2017.
- [7] Kerem C Tezcan, Christian F Baumgartner, Roger Luechinger, Klaas P Pruessmann, and Ender Konukoglu. MR image reconstruction using deep density priors. *IEEE transactions on medical imaging*, 38(7):1633–1642, 2019.
- [8] Guanxiong Luo, Na Zhao, Wenhao Jiang, Edward S. Hui, and Peng Cao. MRI reconstruction using deep bayesian estimation. *Magn. Reson. Med.*, 84(4):2246–2261, apr 2020.
- [9] Qiegen Liu, Qingxin Yang, Huitao Cheng, Shanshan Wang, Minghui Zhang, and Dong Liang. Highly undersampled magnetic resonance imaging reconstruction using autoencoding priors. *Magnetic Resonance in Medicine*, 83(1):322–336, 2020.
- [10] Diederik P Kingma and Max Welling. Auto-encoding variational bayes. *arXiv*, 2014.
- [11] Guillaume Alain and Yoshua Bengio. What regularized auto-encoders learn from the data generating distribution. *arXiv*, 2014.
- [12] Tim Salimans, Andrej Karpathy, Xi Chen, and Diederik P. Kingma. Pixelcnn++: Improving the pixelcnn with discretized logistic mixture likelihood and other modifications. *arXiv*, arXiv:1701.05517, January 2017.

[13] Morteza Mardani, Enhao Gong, Joseph Y Cheng, Shreyas S Vasanawala, Greg Zaharchuk, Lei Xing, and John M Pauly. Deep generative adversarial neural networks for compressive sensing mRI. *IEEE transactions on medical imaging*, 38(1):167–179, 2018.

[14] Charles Blundell, Julien Cornebise, Koray Kavukcuoglu, and Daan Wierstra. Weight Uncertainty in Neural Networks. *arXiv*, 2015.

[15] Dominik Narnhofer, Alexander Effland, Erich Kobler, Kerstin Hammernik, Florian Knoll, and Thomas Pock. Bayesian Uncertainty Estimation of Learned Variational MRI Reconstruction. *arXiv*, 2021.

[16] Ajil Jalal, Marius Arvinte, Giannis Daras, Eric Price, Alexandros G. Dimakis, and Jonathan I. Tamir. Robust compressed sensing mri with deep generative priors. August 2021.

[17] Aapo Hyvärinen. Estimation of non-normalized statistical models by score matching. *Journal of Machine Learning Research*, 6(24):695–709, 2005.

[18] Vincent Pascal. A connection between score matching and denoising autoencoders. *Neural Computation*, 23(7):1661–1674, 2011.

[19] Jascha Sohl-Dickstein, Eric A. Weiss, Niru Maheswaranathan, and Surya Ganguli. Deep unsupervised learning using nonequilibrium thermodynamics. *arXiv*, 2015.

[20] Yang Song and Stefano Ermon. Generative modeling by estimating gradients of the data distribution. *arXiv*, 2020.

[21] Yang Song, Jascha Sohl-Dickstein, Diederik P. Kingma, Abhishek Kumar, Stefano Ermon, and Ben Poole. Score-based generative modeling through stochastic differential equations. *arXiv*, 2021.

[22] Simo Särkkä and Arno Solin. *Applied stochastic differential equations*, volume 10. Cambridge University Press, 2019.

[23] Randal Douc, Eric Moulines, Pierre Priouret, and Philippe Soulier. *Markov chains*, chapter 2, pages 38–41. Springer, 2018.

[24] Xun Huang and Serge Belongie. Arbitrary style transfer in real-time with adaptive instance normalization. *arXiv*, 2017.

[25] Ali Rahimi and Benjamin Recht. Random features for large-scale kernel machines. In J. Platt, D. Koller, Y. Singer, and S. Roweis, editors, *Advances in Neural Information Processing Systems*, volume 20 of *NIPS’07*, page 1177–1184, Red Hook, NY, USA, 2008. Curran Associates, Inc.

[26] Guosheng Lin, Anton Milan, Chunhua Shen, and Ian Reid. Refinenet: Multi-path refinement networks for high-resolution semantic segmentation. *arXiv*, 2016.

[27] Xiaolong Wang, Ross Girshick, Abhinav Gupta, and Kaiming He. Non-local neural networks. In *IEEE Computer Society Conference on Computer Vision and Pattern Recognition*, pages 7794–7803, 2018.

[28] Jure Zbontar, Florian Knoll, Anuroop Sriram, Tullie Murrell, Zhengnan Huang, Matthew J. Muckley, Aaron Defazio, Ruben Stern, Patricia Johnson, Mary Bruno, Marc Parente, Krzysztof J. Geras, Joe Katsnelson, Hersh Chandarana, Zizhao Zhang, Michal Drozdza, Adriana Romero, Michael Rabbat, Pascal Vincent, Nafissa Yakubova, James Pinkerton, Duo Wang, Erich Owens, C. Lawrence Zitnick, Michael P. Recht, Daniel K. Sodickson, and Yvonne W. Lui. fastmri: An open dataset and benchmarks for accelerated mri. *arXiv*, 2019.

[29] M. Uecker, P. Lai, M. J. Murphy, P. Virtue, M. Elad, J. M. Pauly, S. S. Vasanawala, and M. Lustig. ES-PIRiT—an eigenvalue approach to autocalibrating parallel MRI: where SENSE meets GRAPPA. *Magn. Reson. Med.*, 71(3):990–1001, 2014.

[30] Martin Uecker, Sebastian Rosenzweig, H. Christian M. Holme, Moritz Blumenthal, Zhengguo Tan, Xiaojing Wang, Jonathan I. Tamir, and Michael Lustig. mrirecon/bart: version 0.6.00, July 2020. NIH Grant U24EB029240-01.

[31] Martín Abadi, Ashish Agarwal, Paul Barham, Eugene Brevdo, Zhifeng Chen, Craig Citro, Greg S. Corrado, Andy Davis, Jeffrey Dean, Matthieu Devin, Sanjay Ghemawat, Ian Goodfellow, Andrew Harp, Geoffrey Irving, Michael Isard, Yangqing Jia, Rafal Jozefowicz, Lukasz Kaiser, Manjunath Kudlur, Josh Levenberg, Dandelion Mané, Rajat Monga, Sherry Moore, Derek Murray, Chris Olah, Mike Schuster, Jonathon Shlens, Benoit Steiner, Ilya Sutskever, Kunal Talwar, Paul Tucker, Vincent Vanhoucke, Vijay Vasudevan, Fernanda Viégas, Oriol Vinyals, Pete Warden, Martin Wattenberg, Martin Wicke, Yuan Yu, and Xiaoqiang Zheng. TensorFlow: Large-scale machine learning on heterogeneous systems. 2015. Software available from tensorflow.org.

[32] Charles R. Harris, K. Jarrod Millman, Stéfan J. van der Walt, Ralf Gommers, Pauli Virtanen, David Cournapeau, Eric Wieser, Julian Taylor, Sebastian Berg, Nathaniel J. Smith, Robert Kern, Matti Picus, Stephan Hoyer, Marten H. van Kerkwijk, Matthew Brett, Allan Haldane, Jaime Fernández del Río, Mark Wiebe, Pearu Peterson, Pierre Gérard-Marchant, Kevin Sheppard, Tyler Reddy, Warren Weckesser, Hameer Abbasi, Christoph Gohlke, and Travis E. Oliphant. Array programming with NumPy. *Nature*, 585(7825):357–362, September 2020.

[33] Efrat Shimron, Jonathan I. Tamir, Ke Wang, and Michael Lustig. Subtle inverse crimes: Naïvely training machine learning algorithms could lead to overly-optimistic results. *arXiv*, 2021.

[34] Stuart Geman and Donald Geman. Stochastic relaxation, gibbs distributions, and the bayesian restoration of images. *IEEE Transactions on Pattern Analysis and Machine Intelligence*, PAMI-6(6):721–741, 1984.

[35] Stefan Roth and Michael J Black. Fields of experts: a framework for learning image priors. In *IEEE Computer Society Conference on Computer Vision and Pattern Recognition*, volume 2 of *CVPR’05*, pages 860–867, 2005.

[36] Uwe Schmidt, Qi Gao, and Stefan Roth. A generative perspective on MRFs in low-level vision. In *IEEE Computer Society Conference on Computer Vision and Pattern Recognition*, pages 1751–1758, 2010.

Appendices

A Rewrite in terms of posterior

Because the forward diffusion is a Markov process and start at \mathbf{x}_0 , with Bayes’ rule we have

$$q(\mathbf{x}_i \mid \mathbf{x}_{i-1}, \mathbf{x}_0) = q(\mathbf{x}_{i-1} \mid \mathbf{x}_i) \frac{q(\mathbf{x}_i \mid \mathbf{x}_0)}{q(\mathbf{x}_{i-1} \mid \mathbf{x}_0)}. \quad (27)$$

Substituting density function into Equation (27) yields

$$q(\mathbf{x}_{i-1} \mid \mathbf{x}_i, \mathbf{x}_0) = q(\mathbf{x}_i \mid \mathbf{x}_{i-1}) \cdot \frac{q(\mathbf{x}_{i-1} \mid \mathbf{x}_0)}{q(\mathbf{x}_i \mid \mathbf{x}_0)} \quad (28)$$

$$= \frac{1}{\sqrt{(2\pi\beta_i^2)^{Np}}} \cdot \frac{b_i^{2Np}}{b_{i-1}^{2Np}} \exp\left[-\left(\frac{\|\mathbf{x}_i - \mathbf{x}_{i-1}\|^2}{\beta_i^2} + \frac{\|\mathbf{x}_{i-1} - \mathbf{x}_0\|^2}{b_{i-1}^2} - \frac{\|\mathbf{x}_i - \mathbf{x}_0\|^2}{b_i^2}\right)\right]. \quad (29)$$

Let $\frac{b_{i-1}^2 + \beta_i^2}{b_i^2} = 1$, which is satisfied with Equation (5), we have

$$q(\mathbf{x}_{i-1} \mid \mathbf{x}_i, \mathbf{x}_0) = \frac{1}{\sqrt{(2\pi\beta_i^2)^{Np}}} \cdot \frac{b_i^{2Np}}{b_{i-1}^{2Np}} \exp\left[-\left(\frac{\|\mathbf{x}_i - \mathbf{x}_{i-1}\|^2}{\beta_i^2} + \frac{\|\mathbf{x}_{i-1} - \mathbf{x}_0\|^2}{b_{i-1}^2} - \frac{\|\mathbf{x}_i - \mathbf{x}_0\|^2}{b_i^2}\right)\right] \quad (30)$$

$$= \frac{1}{\sqrt{(2\pi\beta_i^2)^{Np}}} \cdot \frac{b_i^{2Np}}{b_{i-1}^{2Np}} \exp\left[-\left(\frac{\|\mathbf{x}_{i-1} - \boldsymbol{\mu}\|^2}{\beta_i^2 \cdot \frac{b_{i-1}^2}{b_i^2}}\right)\right], \quad (31)$$

where

$$\boldsymbol{\mu} = \frac{b_{i-1}^2}{b_i^2} \cdot \mathbf{x}_i + \frac{\beta_i^2}{b_i^2} \cdot \mathbf{x}_0. \quad (32)$$

B KL divergence of two Gaussian distributions

Let $p(\mathbf{x}) = \mathcal{CN}(\boldsymbol{\mu}_1, \sigma_1^2 \mathbf{I})$ and $q(\mathbf{x}) = \mathcal{CN}(\boldsymbol{\mu}_2, \sigma_2^2 \mathbf{I})$ and the KL divergence is defined by

$$D_{\text{KL}}(P \parallel Q) = \int_{-\infty}^{\infty} p(\mathbf{x}) \log\left(\frac{p(\mathbf{x})}{q(\mathbf{x})}\right) d\mathbf{x}.$$

Therefore,

$$\begin{aligned} D_{\text{KL}}(P \parallel Q) &= \int [\log p(\mathbf{x}) - \log q(\mathbf{x})] p(\mathbf{x}) d\mathbf{x} \\ &= \mathbb{E}_{p(\mathbf{x})} \left[Np \log\left(\frac{\sigma_2}{\sigma_1}\right) + \frac{1}{\sigma_2^2} \|\mathbf{x} - \boldsymbol{\mu}_2\|^2 - \frac{1}{\sigma_1^2} \|\mathbf{x} - \boldsymbol{\mu}_1\|^2 \right] \\ &= Np \cdot \log\left(\frac{\sigma_2}{\sigma_1}\right) + \frac{1}{\sigma_2^2} \mathbb{E}_{p(\mathbf{x})} [\|\mathbf{x} - \boldsymbol{\mu}_2\|^2] - 1. \end{aligned}$$

where Np is the dimensionality $n \times n \times 2$. Noting that

$$\|\mathbf{x} - \boldsymbol{\mu}_2\|^2 = \|\mathbf{x} - \boldsymbol{\mu}_1\|^2 + 2\Re(\mathbf{x} - \boldsymbol{\mu}_1)^H(\boldsymbol{\mu}_1 - \boldsymbol{\mu}_2) + \|\boldsymbol{\mu}_1 - \boldsymbol{\mu}_2\|^2$$

we arrive at

$$\begin{aligned} D_{\text{KL}}(P \parallel Q) &= Np \cdot \log\left(\frac{\sigma_2}{\sigma_1}\right) + \frac{1}{\sigma_2^2} (\mathbb{E}_{p(\mathbf{x})} [\|\mathbf{x} - \boldsymbol{\mu}_1\|^2] \\ &\quad + 2\Re(\boldsymbol{\mu}_1 - \boldsymbol{\mu}_2)^H \mathbb{E}_{p(\mathbf{x})} [\mathbf{x} - \boldsymbol{\mu}_1] \\ &\quad + \mathbb{E}_{p(\mathbf{x})} [\|\boldsymbol{\mu}_1 - \boldsymbol{\mu}_2\|^2]) - 1 \\ &= Np \cdot \log\left(\frac{\sigma_2}{\sigma_1}\right) + \frac{\sigma_1^2 + \|\boldsymbol{\mu}_1 - \boldsymbol{\mu}_2\|^2}{\sigma_2^2} - 1. \end{aligned}$$

C Details of Networks

The architecture of RefineNet [26] is U-Net based as shown below. The *ref*, *res*, *rcu*, *msf* and *crp* are abbreviations of refine block, residual block, residual convolution unit, multi-resolution fusion and chained residual pooling.

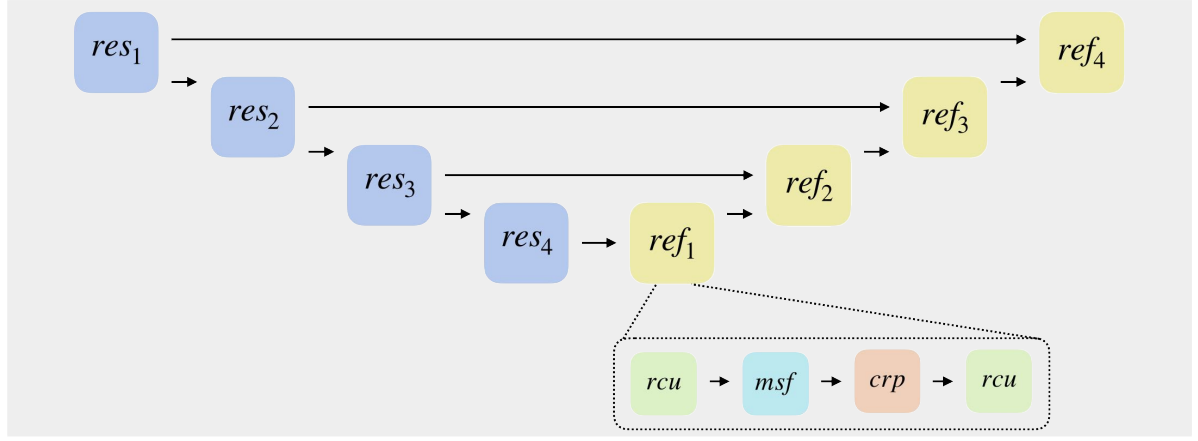


Figure 10. The overview of RefineNet is given above that is U-Net based and refine blocks are used to fuse the multi-scales features.

All the blocks used in the neural networks are conditional on noise scales. For a discrete score network, the conditioning is achieved by instance normalization layers, while in a continuous score network, the conditioning is achieved by adding sinusoidal position embeddings. The discrete score network uses 64 as a base number for filters, while the continuous score network uses 100. The self attention [27] modules are used in the continuous network to capture global information. With our own modifications, all the details are listed in below Table 2.

Table 2. The architectures of score networks.

NET _{1/2}	NET ₃
3x3 Conv2D, filters=64	3x3 Conv2D, filters=100
CondResBlock ₁ , filters=64	CondResBlock ₁ , filters=100
CondResBlock ₁ , filters=64	CondResBlock ₁ , filters=100
CondResBlock ₂ , downsampling filters=128	CondResBlock ₂ , downsampling filters=200
CondResBlock ₂ , filters=128	CondResBlock ₂ , filters=200
CondResBlock ₃ , downsampling, filters=128, dilation=2	CondResBlock ₃ , downsampling, filters=200, dilation=2
CondResBlock ₃ , filters=128 dilation=2	CondResBlock ₃ , filters=200
CondResBlock ₄ , downsampling, filters=128, dilation=4	CondResBlock ₄ , downsampling, filters=200, dilation=4
CondResBlock ₄ , filters=128 dilation=4	CondResBlock ₄ , filters=200
CondRefineBlock ₁ , filters=128	CondRefineBlock ₁ , filters=200
CondRefineBlock ₂ , filters=128	CondRefineBlock ₂ , filters=200
CondRefineBlock ₃ , filters=64	CondRefineBlock ₃ , filters=200
CondRefineBlock ₄ , filters=64	CondRefineBlock ₄ , filters=100
3x3 Conv2D, filters=2 (~7M trainable parameters)	CondRefineBlock ₅ , filters=100 3x3 Conv2D, filters=2 (~27M trainable parameters)

D Hyperparameters for Training

The hyperparameters used for training networks are listed in Table 3. The indexed noise scale is $\sigma_i = \sigma(\frac{i}{N}) = \sigma_{\min}(\frac{\sigma_{\max}}{\sigma_{\min}})^{\frac{i-1}{N-1}}$.

Table 3. Hyperparameters for training

	NET ₁	NET ₂	NET ₃
σ_{\max}	0.3	0.5	0.5
σ_{\min}	0.01	0.01	0.01
N	10	100	100
batch size	10	5	5
embedding size	-	128	200
Fourier scale	-	16	16
learning rate	0.0001	0.0001	0.0001
activation	elu	elu	elu
optimizer	adam	adam	adam

E Grid of Samples

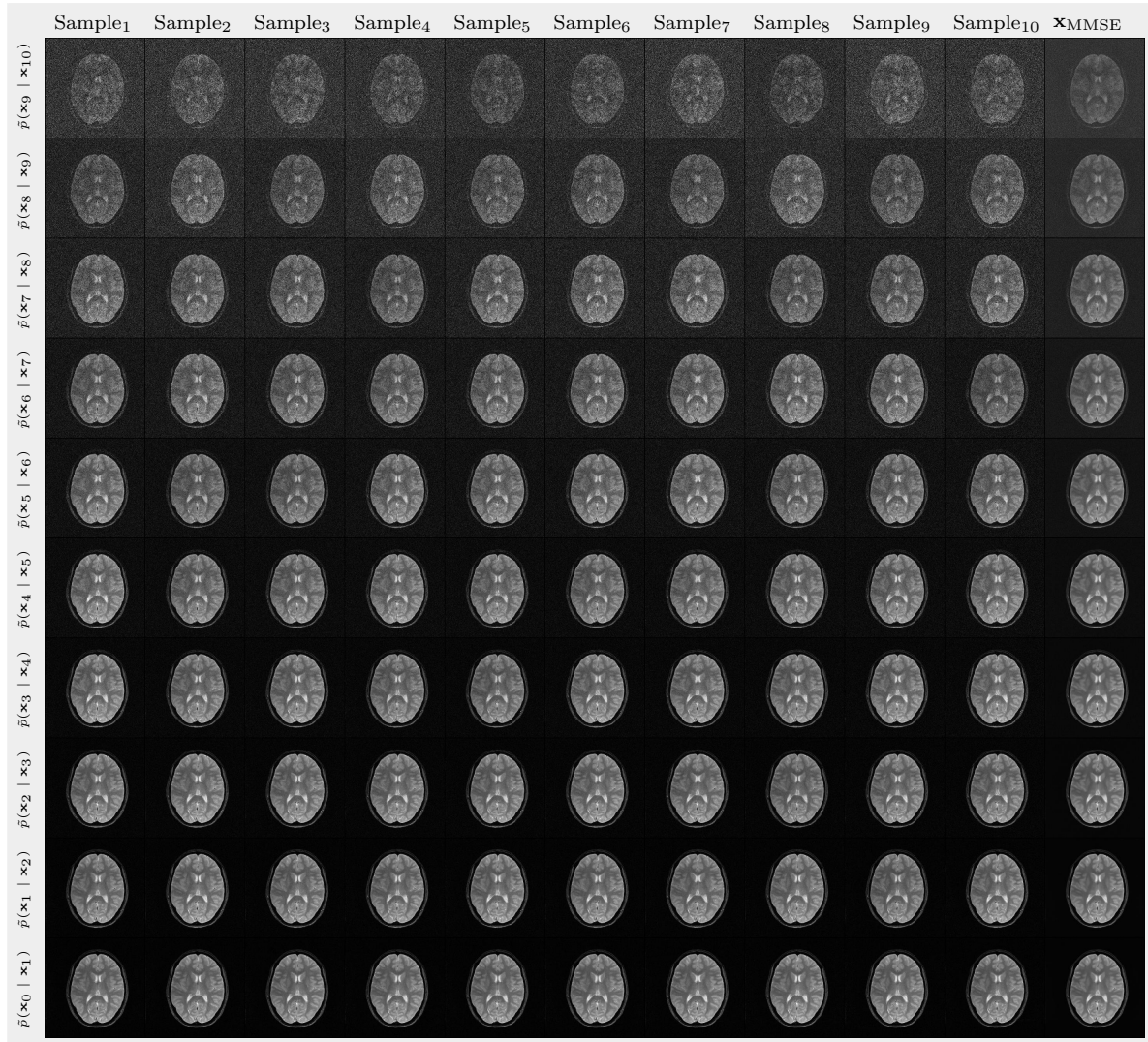


Figure 11. Samples and \mathbf{x}_{MMSE} from intermediate distributions are presented here. Each \mathbf{x}_{MMSE} is the average over 10 samples.